

# Simulation Model for Ultrasonic Motors powered by Resonant Converters

J. Maas, P. Ide, N. Fröhleke, H. Grotstollen

Institute for Power Electronics and Electrical Drives, University of Paderborn, FB 14-LEA  
FAX: 49-5251-603443, Tel. 49-5251-603063, e-mail: jmaas1@columbo.uni-paderborn.de  
33098 Paderborn, Germany

**Abstract**—A rotary traveling wave type ultrasonic motor powered by a resonant converter is modeled to optimize the overall drive performance by simulation and to develop suitable control strategies for the drive. Based on recent mechanical approaches in modeling the stator under consideration of unsymmetries and reflecting the nonlinear stator/rotor-contact by an elastic contact model an extended contact model of the stator/rotor interaction with closed form solutions for non ideal traveling waves is derived referring to a two-mode approximation of the stator and piezoceramic. Incorporation of a converter model into the mechanical subsystem a proper simulation model for ultrasonic drives is presented, whereby some interesting phenomenons are verified by simulations and explained by strong graphical means.

## I. INTRODUCTION

Recently, ultrasonic motors (USMs) have attracted considerable attention as a new type of actuator in servo-systems. USMs combine features such as high driving torque at low rotational speed, high holding torque without an applied electric power, extremely low noise in operation, simple mechanical design and fast response. One of the most advanced USMs is the rotary, traveling wave type motor. In a traveling wave type USM two orthogonal vibration modes are excited to resonance by piezoelectric actuators. Due to the traveling wave the surface points of the stator perform an elliptic motion driving the rotor by frictional force, see [1],[2]. There is an inherent speed reduction to USMs; due to the small tangential velocity of the surface points, the ratio of circular frequency of excitation to rotational speed of the rotor is almost 50000:1. Thus, USMs are suitable to be utilized as gearless actuators or direct servodrives. The electrical excitation of motor vibrations is applied by a voltage-source two-phase inverter. Due to the capacitances of the piezoceramics two series inductors have to be added. Thus, the motor becomes integral part of a resonant converter [3]. USMs are characterized by a two stage energy conversion process. In the first stage, piezoelectric actuators convert high frequency, electri-

cal energy supplied by the feeding converter into mechanical vibration energy of the stator, producing a traveling wave. This process can be assumed as a linear phenomenon. In a second conversion stage the high frequency oscillatory vibration of the stator is rectified into unidirectional rotary motion of the rotor through vibro-impact frictional coupling, which displays the inherent nonlinear behavior of the USM. The total system for the two-phase ultrasonic drive can be divided into its functional components, which are summarized in Fig. 1. In order to optimize the overall drive performance by simulations a detailed model is required. Furthermore the model is essential for developing suitable control strategies.

The publication divides into the following: After a brief modeling review of rotary, traveling wave type USMs a two-phase resonant converter is modeled taking care of some parasitics of the power electronic circuit. The interaction between the feeding converter and the vibrating system is reflected by an electromechanical two-mode approximation for the piezoceramic and stator. Equipped with recent modeling advances of the nonlinear stator/rotor-contact mechanism an extended contact model is derived for non ideal traveling waves, considering interface forces between stator and rotor. After the integration of the just mentioned modeling blocks into one signal flow diagram for the total simulation model of the ultrasonic drive various phenomenons observed on physical drives are verified by simulations. But as the total scheme and the physics behind the contact mechanism is rather complex some graphical means are derived, too, to ease the insight into the motors operation principle.

## II. MODELING OF ULTRASONIC DRIVES

### A. Modeling Review

The conversion of electrical energy into mechanical oscillations which takes place in the piezoelectric ceramic can be discussed on different levels of mathematical modeling. A very general approach holding for arbitrary excitation and waveforms approximates the behavior of the piezoceramics by the linear tensor equations (e-form)

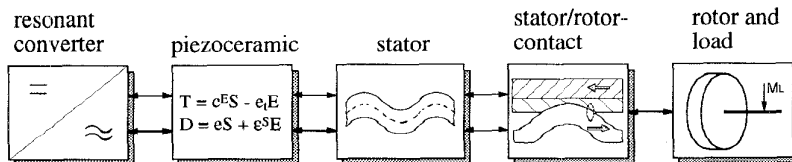


Figure 1: Blockdiagramm for the total system of inverter-fed USM

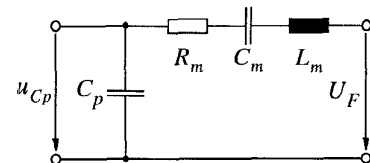


Figure 2: Equivalent circuit model of USM

$$\begin{bmatrix} T \\ D \end{bmatrix} = \begin{bmatrix} c^E & -e_t^T \\ e & \epsilon^S \end{bmatrix} \begin{bmatrix} S \\ E \end{bmatrix}, \quad (1)$$

whereby the mechanical stress tensor  $T$  and the electric displacement vector  $D$  are related to the mechanical strain tensor  $S$  and electric field vector  $E$  via the elastic stiffness tensor  $c^E$ , the piezoelectric stress tensor  $e_t$  (subscript „t“ denotes the transpose of the tensor), and the dielectric permittivity tensor  $\epsilon^S$ .

According to the electromechanical conversion theory of an ultrasonic vibrating system [1] for each phase the equivalent circuit model in Fig. 2 is obtained. Sinusoidal waveforms are assumed for the variables and only transverse effects in the piezoelectric stress tensor  $e$  are considered. The capacitive behavior of the piezoceramic is reflected by  $C_p$ , whereby the mechanical vibrations of the stator are characterized by  $L_m$ ,  $C_m$  and  $R_m$ . The parametrization is performed by a force factor given in [1], expressing the electromechanical coupling. The equivalent electrical voltage  $U_F$  describes the mechanical driving force, which acts as driving quantity via a simplified stator/rotor-contact model on the rotor. In many cases the mechanical load connected to the output terminals is modeled simply by a constant resistor. However, it is already accepted, that the inherent mechanical characteristic of USMs are widely nonlinear, especially, when it comes to reflect the stator/rotor-contact.

Thus, in [1] a more precise approach is presented using nonlinear equivalent components as e.g. a network containing zener diodes to model the stator/rotor-contact. Unluckily, the parametrization of the network requires extensive experiments and turns out to be less practical for an optimization of USMs prior. To overcome this problems in [4] the nonlinear interface between stator and rotor is considered by nonlinear mechanical forces, which are determined by an elastic contact model. The coupling between mechanical forces and the equivalent circuit of the vibrator is performed by using the force factor description as already mentioned.

For the modeling approaches given above a perfect symmetrical motor construction is assumed to yield an ideal motor behavior due to equal phases. Then the two-phase USM can be replaced by two identical equivalent circuits as given by Fig. 2. In practice, mechanical cross-couplings and unsymmetries between both phases do occur and should be taken into account for optimization of ultrasonic drives. Recent available results to model the stator under non ideal conditions [5], [6] by a discrete mechanical two-mode representation base on finite-element methods for the parametrization of the motor. This approach describes the physical phenomenons of rotary, traveling wave type USMs precisely enough for the total drive behavior, since it refers to published contact models for the nonlinear stator/rotor-contact, given in [7], [8], [9].

In [10] a general framework for modeling piezoelectric, rotary, travelling wave type motors is given. Since on one hand a great number of eigenmodes are considered in this approach and on the other hand the stator/rotor-contact is modeled two dimensionally, no closed form solutions can be derived for the contact interface. Simulative investigations are thus very time consuming and are less suitable for the optimization of a controlled drive.

Therefore another model approach is presented in this publication, where the radial dependence of the contact problem is neglected, motivated by the results given in [8]. Then closed form solutions can

be derived, leading to time efficient total system simulations. The effects of the stator geometry and the properties of the piezoceramic on the modeshapes in the relevant contact zone is considered by the model given in [5], [6]. Since the total ultrasonic drive is to be modeled, a converter model is included for the power electronic circuit. Hence, a more suitable and accurate modeling of USMs is feasible, allowing an optimization of the overall drive performance by simulation.

## B. Modeling of the power electronic circuit

Due to the non ideal motor characteristics in practice the feeding two-phase resonant converter must be driven by an adequate quantity of control parameters to attain the best motor performance. In [11] a novel experimental set-up for an ultrasonic prototype drive controlled by a DSP is presented. In order to realize a flexible control scheme for the prototype drive, the authors recommend a fullbridge topology for the inverter stage (see Fig. 3), which is driven by the control quantities: switching frequency  $f_S$ , phase angle  $\phi$  and duty cycles  $\beta_1$  and  $\beta_2$  of both phases, see Fig. 4. The latter take care for independent adjustment of the voltage amplitude. Hence, measures

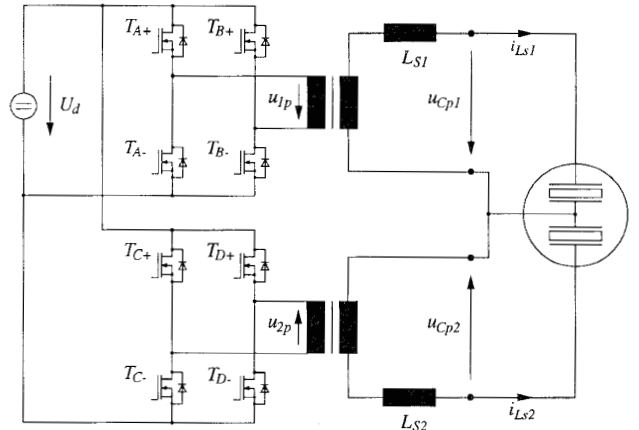


Figure 3: Two-phase resonant converter feeding USM

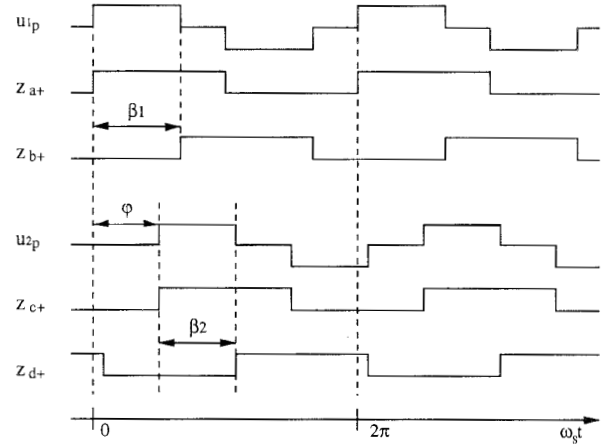


Figure 4: Inverter voltages in accordance with quantities  $f_S$ ,  $\phi$ ,  $\beta_1$ ,  $\beta_2$

against the effects of motor unsymmetries and cross-couplings are given.

For modeling the power electronic circuit the principal circuit depicted in Fig. 3 is used. Due to the symmetrical converter topology only one phase must be described. The function of the inverter is modeled by piecewise-linear voltage sources, controlled by the dc-link voltage  $U_d$ ,  $f_s$ ,  $\phi$  and  $\beta$ . Conduction losses of the inverters MOSFETs are reflected by  $R_{Inv}$  equal to  $2R_{DSon}$ . The transformer with ratio  $1:n_T$  is approximated by an unsymmetrical equivalent circuit model with secondary side parameters  $R_{cu}$ ,  $L_p$ ,  $L_m$ . The inductor  $L_s$  of the resonant tank ( $L_s$ ,  $C_p$ ) is completed by its equivalent series resistance  $R_{Ls}$ , while the capacitive behavior of piezoceramic is reflected by the capacitance  $C_p$ . It is integral part of the resonant tank as mentioned before. The losses of the piezoceramic are considered by  $R_p$ .

For the representation of the inverter it is useful to relate the primary sided quantities to the secondary side, giving:

$$u'_{Inv} = n_T u_{Inv}, \quad i'_{Inv} = 1/n_T i_{Inv}, \quad R'_{Inv} = n_T^2 2R_{DSon}.$$

Thus, each phase of the converter is modeled by a circuit depicted in Fig. 5, with parameters  $R_S = R_{cu} + R_{Ls}$  and  $L'_S = L_l + L_s$ .

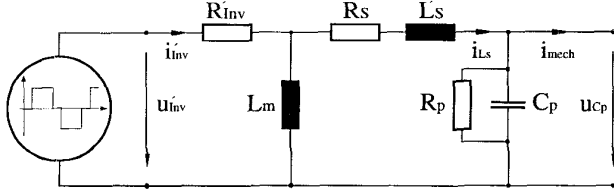


Figure 5: Model for each phase of the two-phase resonant converter

The output quantity of this model is the motor voltage  $u_{Cp}$ , which acts on the mechanical part of the USM via the inverse piezoelectric effect. The reaction from the mechanical subsystem on the inverter is given by the quantity  $i_{mech}$ . The physical behavior of the analog model (Fig. 5) can be formulated by the following state equations:

$$L_m (i_m)' = u'_{Inv} - (i_m + i_{Ls}) R'_{Inv} \quad (2)$$

$$L'_S (i_{Ls})' = u'_{Inv} - i_m R'_{Inv} - (R'_{Inv} + R_S) i_{Ls} - u_{Cp} \quad (3)$$

$$C_p (u_{Cp})' = i_{Ls} - 1/R_p u_{Cp} - i_{mech} \quad (4)$$

These equations are used to set up a signal flow diagram for the drive's control design. It is advantageous not to feed back the current  $i_{mech}$  in (4), but to use the charge  $q_{mech}$  generated by the piezoelectric effect from the mechanical subsystem:

$$q_{Cp} = C_p \int (u_{Cp})' dt = \int (i_{Ls} - 1/R_p u_{Cp}) dt - q_{mech}. \quad (5)$$

Hence, the electrical part can be modeled by two circuits as the one shown in Fig. 5.

### C. Modeling of Piezoceramic and Stator

In [5] an equivalent mechanical two-mode approximation is given, representing the modal amplitudes  $w_{1,t}$ ,  $w_{2,t}$  of the sine- and cosine-mode of the vibrating system (piezoceramic and stator), see Fig. 6. The parameter  $m$  describes the model mass of stator and

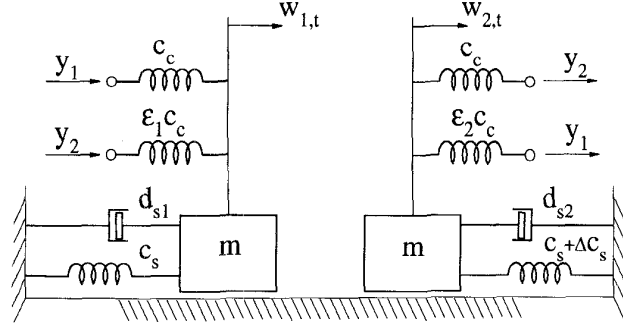


Figure 6: Coupled discrete mechanical model of piezoceramic and stator

ceramic,  $m = m_s + m_c$ ,  $d_s$  reflects the structural damping and  $c_s$  represents the equivalent mechanical stiffness of the stator, whereby the respective ceramic stiffness is given by  $c_c$ .

Each piezoelectric actuator excites this mechanical model via displacements  $y_1$  and  $y_2$ , which are proportional to the phase voltages  $u_{Cp1}$  and  $u_{Cp2}$  of the resonant converter. Unsymmetries by the construction and manufacturing of the stator are taken into account by adding  $\Delta c_s$  in the respective, discrete mechanical system. Since the excitation of the sine- and cosine-mode is almost along a semi circle instead of a complete piezoelectric ring, cross excitation occurs between the two modes, which are considered by the small symmetry disturbances  $\epsilon_1$ ,  $\epsilon_2$ . The determination of the model parameters can be based on energy considerations or detailed finite-element analysis of the vibration system consisting of piezoceramic layer and stator.

In [6] an extensive treatment of the parametrization procedure is presented for the mechanical model (Fig. 6) of the USM by means of finite-element calculation. The modeling takes care of the exact geometry of the stator, including the teeth at the outer ring under use as well as the piezoelectric ceramic by (1). Out of the eigenmode analysis only those double eigenvalues (sine- and cosine-mode of the  $n$ -th eigenmode) are considered for the determination of parameters, which are utilized for driving the rotor. In [12] this procedure is discussed and the parametrization of the model in Fig. 6 is given in detail. Note, the determination of  $y_1$  and  $y_2$ : In [6] an elongation factor  $\hat{A}$  is introduced, yielding the relation between the applied voltage  $u_{Cp}$  and displacement  $y$  by  $y = \hat{A} u_{Cp}$ . Due to the very physical reflection of the electromechanical couplings of the ceramic/stator-system by the finite-element analysis, an accurate determination of parameter  $\hat{A}$  is feasible.

The dynamics of the model in Fig. 6 can be described by the following state equations:

$$\begin{bmatrix} m & 0 \\ 0 & m \end{bmatrix} \begin{bmatrix} \ddot{w}_{1,t} \\ \ddot{w}_{2,t} \end{bmatrix} + \begin{bmatrix} d_{s1} & 0 \\ 0 & d_{s2} \end{bmatrix} \begin{bmatrix} \dot{w}_{1,t} \\ \dot{w}_{2,t} \end{bmatrix} + \begin{bmatrix} c_1 & 0 \\ 0 & c_2 \end{bmatrix} \begin{bmatrix} w_{1,t} \\ w_{2,t} \end{bmatrix} = \begin{bmatrix} \hat{A}_1 c_c & \hat{A}_2 \epsilon_1 c_c \\ \hat{A}_1 \epsilon_2 c_c & \hat{A}_2 c_c \end{bmatrix} \begin{bmatrix} u_{Cp1} \\ u_{Cp2} \end{bmatrix} \quad (6)$$

$$\Leftrightarrow \mathbf{M} \cdot \ddot{\mathbf{w}}_t + \mathbf{D} \cdot \dot{\mathbf{w}}_t + \mathbf{C} \cdot \mathbf{w}_t = \mathbf{\Theta} \cdot \mathbf{u}_t \quad (7)$$

with  $c_1 = c_s + c_c (1 + \epsilon_1)$  and  $c_2 = c_s + \Delta c_s + c_c (1 + \epsilon_2)$ .

$\Theta$  represents the electromechanical coupling matrix considering the cross excitation.  $c_1$  and  $c_2$  reflect the effective modal stiffness. Equation (7), describing the mechanical subsystem, is identical to the actuator equation in [10]. There the electrical part of the piezoelectric ceramic is expressed by

$$\Theta^T \cdot \mathbf{w}_t + \mathbf{C}_p \cdot \mathbf{u} = \mathbf{q}, \quad (8)$$

the so called sensor equation. For the electromechanical total system, (8) represents the effects on the power supply, with

$$\Theta^T \cdot \mathbf{w}_t = \begin{bmatrix} \hat{A}_1 c_C & \hat{A}_1 \varepsilon_2 c_C \\ \hat{A}_2 \varepsilon_1 c_C & \hat{A}_2 c_C \end{bmatrix} \begin{bmatrix} w_{1,t} \\ w_{2,t} \end{bmatrix} = \begin{bmatrix} q_{1mech} \\ q_{2mech} \end{bmatrix},$$

being the generated charges by the piezoelectric effect from the mechanical subsystem (taking care of cross couplings), with

$$\mathbf{q}_{Cp} = \mathbf{C}_p \cdot \mathbf{u} = \begin{bmatrix} C_{p1} & 0 \\ 0 & C_{p2} \end{bmatrix} \begin{bmatrix} u_{Cp1} \\ u_{Cp2} \end{bmatrix},$$

describing the dielectric properties of the piezoceramic and

$$\mathbf{q}^T = [q_1 \ q_2],$$

the charges, supplied by the feeding converter. If (8) is extended by the losses of the piezoelectric actuators, each row of the mathematical description is identical to (5). Hence, the coupling of the two-phase resonant converter and the mechanical system is completed.

The modal amplitudes  $\mathbf{w}_t^T = [w_{1,t} \ w_{2,t}]$  belong to the  $n$ -th eigenmode  $\Phi_{\hat{x}} = [\sin k\hat{x} \ \cos k\hat{x}]$  of the vibrating system:

$$w_1(\hat{x}, t) = w_{1,t} \cdot \sin k\hat{x} \quad (\text{sine-mode}), \quad (9)$$

$$w_2(\hat{x}, t) = w_{2,t} \cdot \cos k\hat{x} \quad (\text{cosine-mode}), \quad (10)$$

with  $k = 2\pi/\lambda$  and  $\lambda$  the wavelength of the  $n$ -th mode.

Under simplifying assumptions [8], (9) and (10) describe the transverse displacements of the stator's middle surface line in the very narrow contact zone between stator and rotor at the radius,  $r = R_w$ . The resonant traveling wave

$$w(\hat{x}, t) = \Phi_{\hat{x}} \cdot \mathbf{w}_t = w_{1,t} \cdot \sin k\hat{x} + w_{2,t} \cdot \cos k\hat{x} \quad (11)$$

results from the superposition of the sine-mode (9) and cosine-mode (10). The displacement of a surface point  $Q$  of the stator ( $r = R_w$ ) can be written as

$$\vec{w}_Q(\hat{x}, t) = w(\hat{x}, t) \vec{e}_z - a \frac{\partial}{\partial \hat{x}} w(\hat{x}, t) \vec{e}_{\hat{x}}, \quad (12)$$

where the first term refers to the vertical motion and the second term refers to the tangential motion. The distance between the plate's surface and the center line is expressed by  $a$ . The tangential velocity  $v_h(\hat{x}, t)$  of a surface point is given by time derivation

$$v_h(\hat{x}, t) = -a \frac{d}{dt} \frac{\partial w(\hat{x}, t)}{\partial \hat{x}}. \quad (13)$$

The interaction of vertical displacement  $w(\hat{x}, t)$  and tangential velocity  $v_h(\hat{x}, t)$  of the stator's surface points drives the rotor by frictional force along the region of mechanical contact between stator and rotor. The stator/rotor-contact mechanism responsible for the tangential force is quite complicated.

In order to consider the interaction between the stator/rotor-contact, equation (7) reflecting the stator's dynamics is to extend by two nonlinear modal forces  $\mathbf{F}_d^T = [F_{d1} \ F_{d2}]$  yielding

$$\mathbf{M} \cdot \ddot{\mathbf{w}}_t + \mathbf{D} \cdot \dot{\mathbf{w}}_t + \mathbf{C} \cdot \mathbf{w}_t = \Theta \cdot \mathbf{u} + \mathbf{F}_d. \quad (14)$$

#### D. Stator/Rotor-Contact Mechanism

Recently, approaches on modeling the stator/rotor-contact mechanism [7], [8], [9] were published, which are useful to generate a simulation model for ultrasonic drives.

Reactions from the rotor to the stator are neglected. Sinusoidal waveforms are assumed for the modal amplitudes  $w_{1,t}$  and  $w_{2,t}$ .

$$w_1(\hat{x}, t) = \hat{w}_1 \cdot \sin k\hat{x} \cdot \sin \omega t \quad (15)$$

$$w_2(\hat{x}, t) = \hat{w}_2 \cdot \cos k\hat{x} \cdot \sin(\omega t + \varphi_m), \quad (16)$$

with  $\omega$ , the angular frequency and  $\varphi_m$  as phase angle between the modes. In addition, it is assumed that  $\hat{w}_1 = \hat{w}_2 = \hat{w}$  and  $\varphi_m$  equals  $90^\circ$ , yielding an ideal right moving traveling wave in the stator

$$w(\hat{x}, t) = \hat{w} \cos(k\hat{x} - \omega t). \quad (17)$$

The tangential velocity of a surface point in (13) can be described for an ideal traveling wave by

$$v_h(\hat{x}, t) = -\hat{w} k \omega \cdot \cos(k\hat{x} - \omega t) = \hat{v}_h \cdot \cos(k\hat{x} - \omega t). \quad (18)$$

The description of the contact mechanism in the coordinate system of the stator is due to the time related terms in (17) and (18) disadvantageous. Since the contact mechanism is assumed to be basically stationary for an ideal traveling wave, it seem to be suitable to introduce a coordinate system moving with the traveling wave. It is oriented towards an arbitrary wave crest of the traveling wave and originates at  $x = 0$ . Between a fixed coordinate system on the stator and a moving coordinate system the transformation relation holds:  $x = \hat{x} - \omega/k \cdot t$ . Thus, for the vertical displacement and the horizontal velocity the following relations result from (17) and (18):

$$w(x) = \hat{w} \cdot \cos(kx), \quad v_h(x) = \hat{v}_h \cdot \cos(kx). \quad (19)$$

A contact mechanism for an arbitrary „wave hill“ is displayed in Fig. 7a in a transformed coordinate system as in [7]. The stator is assumed to be rigid while the elastic contact layer of the rotor is modeled as a linear spring with equivalent stiffness  $c_N$ , defined as

$$c_N = Eb/h_r, \quad (20)$$

where  $E$  is Young's modulus of the contact layer,  $h_r$ , the thickness of the contact layer and  $b$ , the contact width in radial direction. The overlap  $\Delta w$  between the rotor and the stator is given by  $\Delta w = \hat{w}(\cos kx - \cos kx_0)$ , resulting to a normal contact pressure distribution along the contact region  $-x_0 \leq x \leq x_0$  of

$$p(x) = c_N \cdot \Delta w = c_N \cdot \hat{w}(\cos kx - \cos kx_0). \quad (21)$$

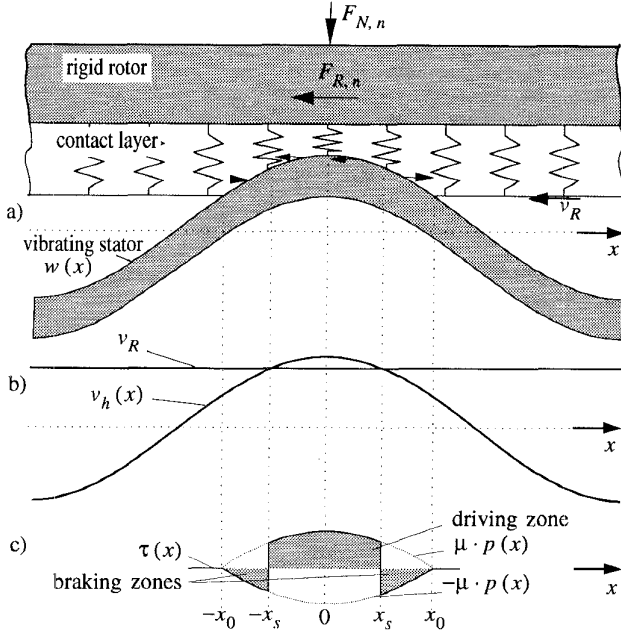


Figure 7: a) Contact mechanism for a rigid stator and elastic contact layer [7]  
b) Distribution of stator velocity  $v_h(x)$  and rotor velocity  $v_R$ .  
c) Distribution of tangential stresses  $\tau(x)$ .

Coulombs's friction law is assumed between stator and rotor, modeling only slip effects by the coefficient  $\mu$ , assumed as constant. Thus, the tangential stresses  $\tau(x)$  along the contact region are calculated by

$$\tau(x) = \text{sgn}(|v_h(x)| - |v_R|) \cdot \mu \cdot p(x), \quad (22)$$

where the sign of  $\tau(x)$  is related to the velocity  $v_h$  of the stator and to the tangential velocity of the rotor  $v_R$  at radius  $r = R_w$ . The driving force of the rotor per wave hill  $F_{R,n}$  is determined by integrating  $\tau(x)$  over the contact zone  $-x_0 \leq x \leq x_0$  of the wavehill.

$$F_{R,n} = \int_{-x_0}^{x_0} \tau(x) dx = 2\mu \int_0^{x_0} \text{sgn}(|v_h(x)| - |v_R|) \cdot p(x) dx \quad (23)$$

For the stick points  $\pm x_s$ , see Fig. 7b, holds  $|v_h(x)| = |v_R|$ . At this specific points a sudden alteration of the tangential stresses from driving force to braking force or reverse occurs. The resulting distribution of the tangential stresses (22) is illustrated in Fig. 7c. From (23) and with contact radius  $R_w$ , the motor torque  $M_R$  under steady state is calculable as  $M_R = n \cdot R_w \cdot F_{R,n}$ .

#### E. Extended Stator/Rotor-Contact Model for Non Ideal Traveling Waves and Rotor Dynamics

For the contact model presented so far ideal traveling waves are assumed described by (17). In order to investigate the drive's behavior in the absence of ideal conditions and to set up a model for the design of the drive's control extensions are required, which reflect the general case with a non ideal traveling wave. The framework outlined in [10] considers principally the general case, but since the contact problem is modeled two dimensionally by non linear equations,

where the latter are to be solved by spatial integration during a transient analysis simulation from step to step, the approach leads to very time consuming simulations. The model presented as follows, which is true for the general case, too, is based on the contact mechanism of [7], see Fig. 7, but because of deriving closed form solutions for the contact interface it is more suitable for transient analysis.

1) *Non ideal traveling wave:* In general the non ideal traveling wave results by the superposition of sine- and cosine-mode (11). Since the contact mechanism shows a nonlinear character as mentioned above, a separate treatment in two counter-rotating systems is prohibited, as the superposition principle is not applicable. Hence, the interaction between stator and rotor is to be investigated in total.

First, for the general case the elliptical trajectories of the surface points are examined, which can be determined by (12). The main axes of the ellipses are no longer orthogonal to the  $\hat{x}$ - $z$  coordinate system as this is true for the ideal traveling wave. For illustration purpose sinusoidal waveforms are assumed for the modal amplitudes  $w_{1,t}$  and  $w_{2,t}$ , referring to (15), (16). But their amplitudes  $\hat{w}_1, \hat{w}_2$  respectively phase  $\phi_m$  differ from the case under ideal conditions. Fig. 8 illustrates the case of differing amplitudes  $\hat{w}_1 \neq \hat{w}_2$  while Fig. 9 illustrates the case with phase  $\phi_m \neq 90^\circ$ . The resulting ellipses are periodic with  $\lambda/2$ , what can be also shown mathematically. In respect to the main axes the presented shapes are schematisized, i.e. the horizontal displacement is far less than the vertical displacement.

During the propagation of a non ideal traveling wave a peak of a „wavehill“ travels through the amplitude maxima of the ellipses shown in Fig. 8 and Fig. 9. It is obvious, that the amplitude of the traveling wave  $w(\hat{x}, t)$  together with the amplitude of the horizontal velocity  $v_h(\hat{x}, t)$  undergo a modulation with time. Note, that the amplitude maxima in vertical direction occur in conjunction with the minima of the amplitude in horizontal direction at  $\hat{x} = \pm\lambda/4$  in Fig. 8 and at  $\hat{x} = \lambda/8$  in Fig. 9 and vice versa at  $\hat{x} = 0$  in Fig. 8 and at  $\hat{x} = -\lambda/8$  in Fig. 9.

Using trigonometric relations, (11) and (13) can be rearranged to

$$w(\hat{x}, t) = \sqrt{w_{1,t}^2 + w_{2,t}^2} \cdot \cos\left(k\hat{x} - \arctan\frac{w_{1,t}}{w_{2,t}}\right), \quad (24)$$

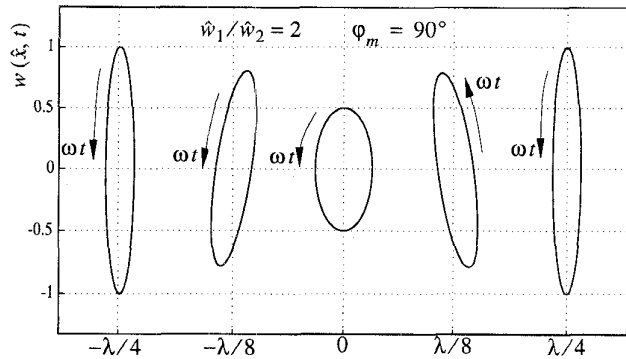


Figure 8: Normalized trajectory of the stator's surface points at  $\hat{x} = \pm\lambda/4$ ,  $\hat{x} = \pm\lambda/8$  and  $\hat{x} = 0$ . A variation of the modal amplitudes alters the amplitudes of the main axes of the ellipses as well as their inclination in the coordinate system. The inclination and the amplitude variation is related to the locus but not to time, which means that the orbit of a surface point does not vary.

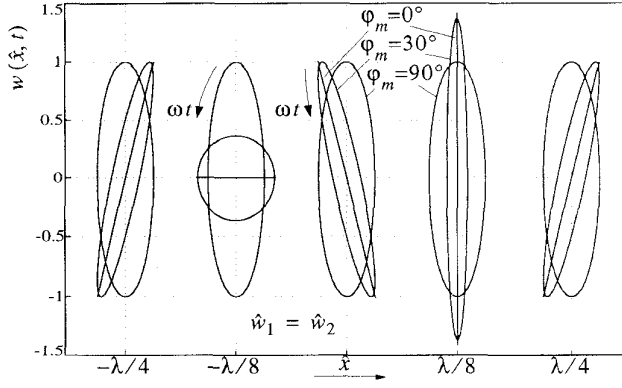


Figure 9: Effects of the phase angle  $\phi_m$  on the elliptical orbit of the surface points (normalized) for  $\hat{w}_1 = \hat{w}_2$ . At  $\phi_m = 0^\circ$ , resulting in a standing wave the ellipses converge to a straight line pointing to the direction of vibration. At  $\phi_m = 90^\circ$ , resulting in an ideal traveling wave, the elliptical trajectory is homogenous and directed perpendicular. At  $\phi_m = 30^\circ$ , resulting in a locus related inclination of ellipses and a variation of the amplitudes of the main axes.

$$v_h(\hat{x}, t) = -ak\sqrt{\dot{w}_{1,t}^2 + \dot{w}_{2,t}^2} \cdot \cos\left(k\hat{x} + \text{atan}\frac{\dot{w}_{2,t}}{\dot{w}_{1,t}}\right). \quad (25)$$

The displacement  $w(\hat{x}, t)$  propagates as transverse wave, while the horizontal velocity wave  $v_h(\hat{x}, t)$  can be viewed as longitudinal wave. As the rotor position in respect to the stator is not of any meaning (section D) a transformation of (24), (25) into a coordinate system moving with the speed of the traveling wave is introduced, which is oriented to an arbitrary maximum of a traveling wave:

$$x = \hat{x} - \frac{1}{k} \text{atan}\frac{\dot{w}_{1,t}}{\dot{w}_{2,t}}. \text{ Hence, we obtain} \quad (26)$$

$$w(x, t) = \sqrt{\dot{w}_{1,t}^2 + \dot{w}_{2,t}^2} \cdot \cos kx = \hat{w}(t) \cdot \cos kx \quad (27)$$

$$v_h(x, t) = -ak\sqrt{\dot{w}_{1,t}^2 + \dot{w}_{2,t}^2} \cdot \cos(kx + kx_c(t)) = \hat{v}_h(t) \cdot \cos(kx + kx_c(t)), \quad (28)$$

$$\text{with } kx_c = \text{atan}\frac{\dot{w}_{1,t}\dot{w}_{1,t} + \dot{w}_{2,t}\dot{w}_{2,t}}{\dot{w}_{2,t}\dot{w}_{1,t} - \dot{w}_{1,t}\dot{w}_{2,t}}, \quad (29)$$

the phase shift between vertical displacement and horizontal velocity. It becomes obvious when inspecting (29), that not only  $\hat{w}(t)$  and  $\hat{v}_h(t)$  vary with time, but also  $kx_c(t)$ . This fact has a major impact on the contact mechanism. For ideal conditions (19)  $\hat{w}$  and  $\hat{v}_h$  are constant and  $x_c$  equals 0.

2) *Torque generation and modal forces:* Due to the non ideal traveling wave (27), (28), (29) no symmetrical contact mechanism occurs, see Fig. 10, as given for the ideal case in Fig. 7. Evaluating integral (23) no simplification by symmetry can be used. The left and right sided stick points  $x_{sl}$  and  $x_{sr}$ , which are positive defined in Fig. 10 differ generally and vary with time. The separation between the stator surface at  $w = 0$  and undeformed contact layer is defined by

$$w_R(t) = \hat{w}(t) \cdot \cos kx_0. \quad (30)$$

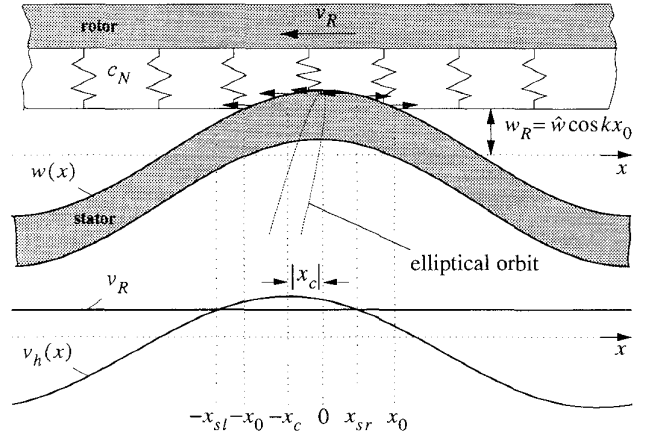


Figure 10: Stator/rotor-contact for the non ideal traveling wave. The displacement  $x_c$  is unequal to zero and causes an unsymmetrical contact mechanism with  $\hat{w}$  and  $\hat{v}_h$  occurring at different loci.

The following relation is true for the driving force:

$$F_R = n\mu \int_{-x_0}^{x_0} \text{sgn}(|v_h(x)| - |v_R|) \cdot p(x) dx, \quad (31)$$

whereby here we assume that the wave travels in the  $\hat{x}$  direction and the rotor moves in the  $-\hat{x}$  direction. The direction of the tangential velocity  $v_h$  at the maximum of the traveling wave is to be considered later. The actual direction of the surface points  $d_{sp}$  is lost by the transformation into the moving coordinate system. For the purpose of simplification of (31) relation  $\phi_r(x)$  is introduced:

$$\phi_r(x) = k \int (\cos kx - \cos kx_0) dx = \sin kx - kx \cos kx_0.$$

For the simulation model of the overall drive, feedback effects of the stator/rotor-contact on the stator's vibration is included as compared to [7], [8], [9]. There are two forces acting along the contact region and must be considered for the dynamics of the vibrator (14) by a modal forcing vector  $\mathbf{F}_d$ . From the stator's deflection in normal direction a feedback of the contact interface is given by a normal forcing vector  $\mathbf{F}_{dn}$  [10]:

$$\mathbf{F}_{dn} = -n \int_{-x_0}^{x_0} \Phi_{\hat{x}}^T \cdot p(x) dx. \quad (32)$$

In tangential direction the contact acts to the stator's dynamic by a forcing vector  $\mathbf{F}_{dt}$  due to the tangential surface deflection [10]:

$$\mathbf{F}_{dt} = -n\mu a \int_{-x_0}^{x_0} \frac{\partial \Phi_{\hat{x}}^T}{\partial \hat{x}} \cdot \text{sgn}(|v_h(x)| - |v_R|) \cdot p(x) dx. \quad (33)$$

With  $\Phi_{\hat{x}} = [\sin k\hat{x} \cos k\hat{x}]$ , (21), (26) and (27) an explicit description is obtained for the nonlinear forcing vectors in (32) and (33):

$$\mathbf{F}_{dn} = -n \frac{c_N}{k} \begin{bmatrix} w_{1,t}(kx_0 - 1/2 \sin 2kx_0) \\ w_{2,t}(kx_0 - 1/2 \sin 2kx_0) \end{bmatrix}$$

and for simplification of (33) the analytical relations

$$\Phi_s(x) = k\hat{w} \int \begin{bmatrix} \cos k\hat{x} \\ -\sin k\hat{x} \end{bmatrix} p(x) dx = \begin{bmatrix} w_{1,t}\phi_e + w_{2,t}\phi_o \\ w_{2,t}\phi_e - w_{1,t}\phi_o \end{bmatrix} = [\Phi_e + \Phi_o],$$

with  $\phi_e(x) = 1/4 \cos 2kx - \cos kx \cdot \sin kx_0$ ,

$$\phi_o(x) = 1/2 kx + 1/4 \sin 2kx - \sin kx \cdot \cos kx_0.$$

No case separation is necessary for the calculation of the normal forcing vector  $\mathbf{F}_{dn}$  (32). When calculating the tangential forcing vector  $\mathbf{F}_{dt}$  (33) and the driving force  $F_R$  (31) a separate evaluation for diverse cases of the contact mechanism has to be conducted, affected by the sign function.

- 1)  $x_{sl} \leq x_0$  and  $x_{sr} \leq x_0$ : As the stick points  $x_{sl}$  and  $x_{sr}$  are located inside the contact region, 3 zones are to be considered. In the outer zones frictional forces cause a braking effect; in the intermediate interval a driving action results. The driving force and the tangential force vector is calculated by:

$$F_R = n\mu \frac{c_N}{k} 2\hat{w} (\phi_r(x_{sr}) + \phi_r(x_{sl}) - \phi_r(x_0)),$$

$$\mathbf{F}_{dt} = -n\mu ac_N 2 (\Phi_s(x_{sr}) - \Phi_s(-x_{sl}) - \Phi_o(x_0)).$$

- 2)  $x_{sl} > x_0$  and  $x_{sr} \leq x_0$ : This contact case containing a driving and a slowing zone is presented in Fig. 10, with

$$F_R = n\mu \frac{c_N}{k} 2\hat{w} \phi_r(x_{sr}), \quad \mathbf{F}_{dt} = -n\mu ac_N 2 (\Phi_s(x_{sr}) - \Phi_e(x_0)).$$

- 3)  $x_{sl} \leq x_0$  and  $x_{sr} > x_0$ : The counter part to case 2, with

$$F_R = n\mu \frac{c_N}{k} 2\hat{w} \phi_r(x_{sl}), \quad \mathbf{F}_{dt} = -n\mu ac_N 2 (-\Phi_s(-x_{sl}) + \Phi_e(x_0)).$$

- 4)  $x_{sl} > x_0$  and  $x_{sr} > x_0$ : The pressure distribution causes only a driving effect. Thus, we obtain:

$$F_R = n\mu \frac{c_N}{k} 2\hat{w} \phi_r(x_0), \quad \mathbf{F}_{dt} = -n\mu ac_N 2 \Phi_o(x_0).$$

- 5)  $|v_R| > |\hat{v}_h|$ , no stick points  $x_s$ : If the magnitude of the horizontal velocity of the stator's surface points is smaller than the rotor velocity, which means that the motor is to slow down by small modal amplitudes (e.g., if the power supply is switched off), then the frictional force affects a slowing down.

$$F_R = -n\mu \frac{c_N}{k} 2\hat{w} \phi_r(x_0), \quad \mathbf{F}_{dt} = n\mu ac_N 2 \Phi_o(x_0).$$

In order to consider the information about the effect of the traveling wave, the actual direction of the surface points  $d_{sp}$  at the wave crest is to be inserted into the equations above, since the drive should be modeled in both directions. Hence, for the torque  $M_R$  of the ultrasonic drive with radius  $r = R_w$  and modal forcing vector  $\mathbf{F}_d$ , we obtain:

$$M_R = d_{sp} R_w F_R, \quad (34)$$

$$\mathbf{F}_d = \mathbf{F}_{dn} + d_{sp} \mathbf{F}_{dt} = \begin{bmatrix} F_{d1} & F_{d2} \end{bmatrix}^T. \quad (35)$$

For ascertaining the actual direction  $d_{sp}$ , (24) is reused. Because  $d_{sp}$  results at the positive maximum of the cos-function, we get  $\hat{x}_m$ , which is to be substituted into (25):

$$\hat{x}_m = \frac{1}{k} \operatorname{atan} \frac{w_{1,t}}{w_{2,t}} \Rightarrow v_h(\hat{x}_m) = -ak \frac{\dot{w}_{1,t} w_{2,t} - \dot{w}_{2,t} w_{1,t}}{\sqrt{w_{1,t}^2 + w_{2,t}^2}}.$$

The actual direction  $d_{sp}$  of the surface points equals the sign of the numerator of  $v_h(\hat{x}_m)$

$$d_{sp} = -\operatorname{sgn}(\dot{w}_{1,t} w_{2,t} - \dot{w}_{2,t} w_{1,t}). \quad (36)$$

Half of the contact zone length  $x_0$  is determined with (30). For the calculation of the stick points  $x_{sl}$  and  $x_{sr}$  (28) and (29) are used again, to yield the stick points with

$$|v_R| \equiv |v_h(x_s)| = |\hat{v}_h| \cos(kx_s + kx_c) \quad \text{to} \\ x_{sr} = \frac{1}{k} \operatorname{acos} \left( \left| \frac{v_R}{\hat{v}_h} \right| \right) - x_c, \quad x_{sl} = \frac{1}{k} \operatorname{acos} \left( \left| \frac{v_R}{\hat{v}_h} \right| \right) + x_c. \quad (37)$$

The stick points vary with time generally;  $x_{sl}$  equals  $x_{sr} + 2x_c$ .

3) *Rotor dynamics*: In dealing with the dynamics of the rotor, two degrees of freedom must be taken into account: First the rotation of the rotor and second the motion in  $z$  direction, as shown by [10].

The motion in  $z$ -direction is represented in Fig. 10 by state quantity  $w_R$ , given by (30). The dynamics of the vertical rotor motion is obtained through the force equilibrium in  $z$  direction:

$$m_R \ddot{w}_R + d_Z \dot{w}_R = n \int_{-x_0}^{x_0} c_N p(x) dx - F_N \\ = 2n(c_N/k) \hat{w} \phi_r(x_0) - F_N = F_Z - F_N, \quad (38)$$

with  $m_R$ , the mass of the rotor and  $d_Z$ , an appropriate damping term of the vertical motion. A part of  $F_Z$  describes the stiffness term in (38). The equation of rotational motion is calculated by

$$J \dot{\omega}_R = M_R - M_L, \quad (39)$$

where  $M_L$  is the applied torque (mechanical load) and  $J$  represents the inertia of the drive. The rotor velocity  $v_R$  equals  $\omega_R R_w$ .

Hence, the stator/rotor-interface and the dynamics of the rotor is completed. An integration of this modeling approach based on closed form solutions for the contact mechanism into the simulation model is feasible.

### III. SIMULATION

#### A. Representation of the Model in a Signal Flow Diagram

Summarizing the models explained in the previous sections for the resonant converter (2), (3), (5), for the piezoceramic and stator (8), (14), for the extended contact model (34), (35) and the rotor model (38), (39), we obtain the signal flow diagram of Fig. 11, reflecting the electromechanical total system. Thus, an efficient simulation model for optimization of the overall ultrasonic drive performance is

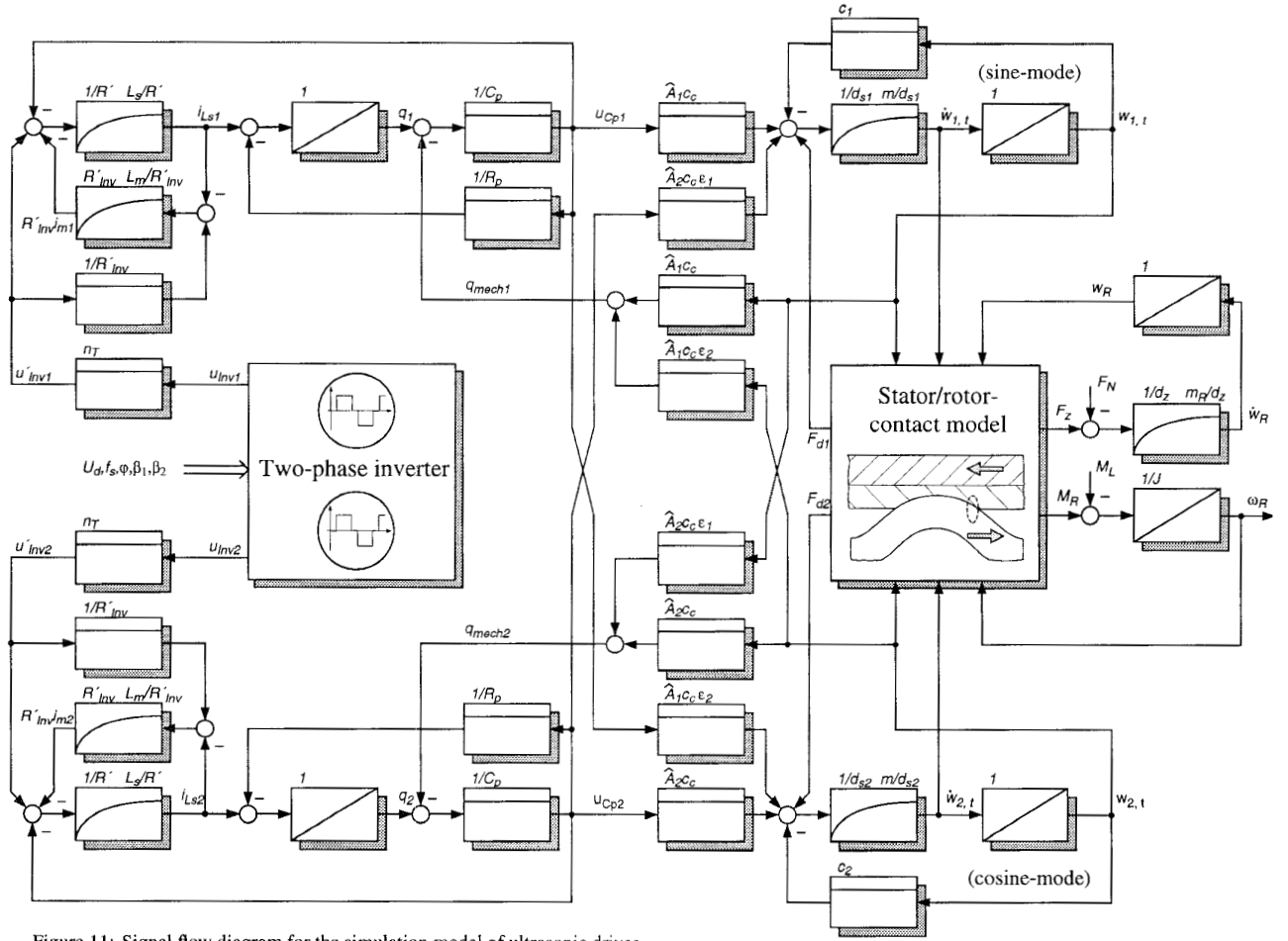


Figure 11: Signal flow diagram for the simulation model of ultrasonic drives

obtained. The implementation is performed on the multi-level simulator SABER and the parameters of a prototype drive [6] are scheduled in Table I, see Appendix.

### B. Simulation Results

The operation of the power converter is illustrated in Fig. 12. The rectangular inverter voltages  $u'_{inv1}$  and  $u'_{inv2}$  are applied to the electrical resonant tank circuits. With a proper design of  $L_S$  sinusoidal waveforms are obtained for the phase voltages  $u_{cp1}$  and  $u_{cp2}$  required for feeding of the USM. Due to the lagging power factor operation mode the charge-down losses in the power MOSFETs are eliminated verified by measurements for a prototype drive in [11].

The effects of symmetry disturbances considered by parametrization of the USM (see Table I) on the behavior of the vibrating stator are depicted in Fig. 13. In case a) the unsymmetrical motor is fed by symmetrical inverter voltages ( $\beta_1 = \beta_2$ ,  $\varphi = 90^\circ$ ). The USM reacts with two different amplitudes  $\hat{w}_1$  and  $\hat{w}_2$  of the modal amplitudes and a phase shift  $\varphi_m \neq 90^\circ$ , which means that an ideal traveling wave does not result. Then in case b), a correction is performed by an unsymmetrical adjustment of the inverter voltages  $u'_{inv1}$  and  $u'_{inv2}$  concurrent with the control parameters in Fig. 12. As a result the

amplitudes  $\hat{w}_1$  and  $\hat{w}_2$  equalize and a phase shift of  $\varphi_m = 90^\circ$  is realized. Thus, an ideal traveling wave is obtained. Hence, the con-

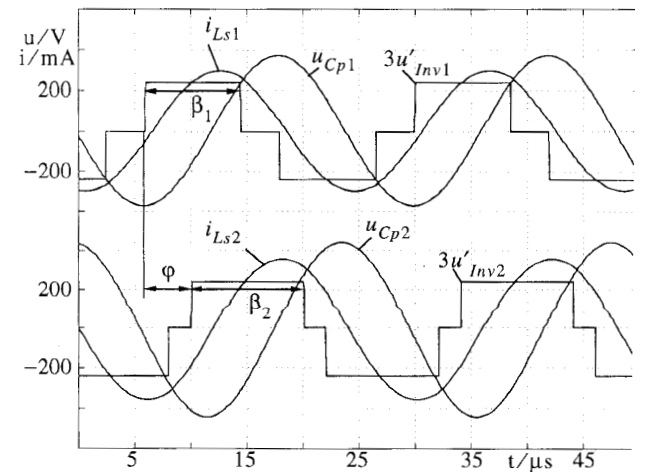


Figure 12: Inverter and phase voltages and phase currents of the resonant converter at steady state for operating point  $f_s = 41.6 \text{ kHz}$ ,  $\beta_1 = 128^\circ$ ,  $\beta_2 = 150^\circ$ ,  $\varphi = 62^\circ$ .



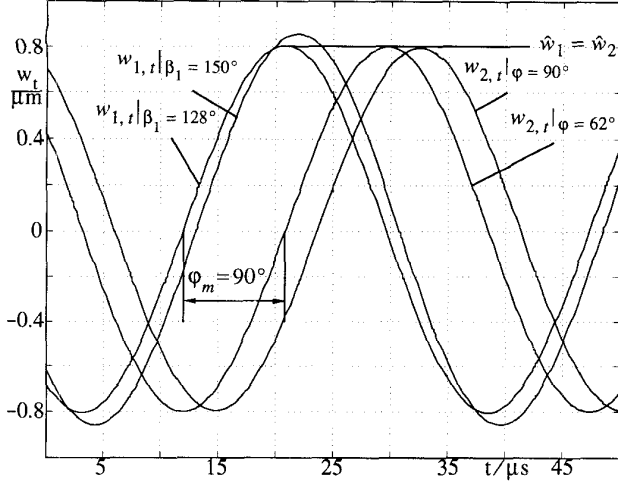


Figure 13: Modal amplitudes  $w_{1,r}, w_{2,t}$  at steady state and  $f_s = 41.6 \text{ kHz}$   
a)  $\beta_1 = \beta_2 = 150^\circ, \varphi = 90^\circ$  with  $w_{1,t} | \beta_1 = 150^\circ, w_{2,t} | \varphi = 90^\circ$   
b)  $\beta_1 = 128^\circ, \beta_2 = 150^\circ, \varphi = 62^\circ$  with  $w_{1,t} | \beta_1 = 128^\circ, w_{2,t} | \varphi = 62^\circ$

verter concept of Fig. 3 proves as proper means to compensate unsymmetries and to optimize the mode of operation by adjusting unsymmetrical control quantities.

In Fig. 14 some simulated characteristic quantities for the contact mechanism and the calculated torque are given for the non ideal traveling wave. By means of a proper selection of control parameters for the converter a non ideal traveling wave ( $\varphi_m \neq 90^\circ, \hat{w}_1 = \hat{w}_2$ ) is obtained, whereby the drive is loaded by  $M_L = 5 \text{ Nm}$ . Note, the enormous alteration of the stick points  $x_{sl}$  and  $x_{sr}$  with the first harmonic of  $2f_s$  according to the variation of the ellipses in Fig. 9. Contrary to the latter half of the contact length  $x_0$  varies only by a small amount, related to the modulation of  $\hat{w}(t)$ . Case 1 to 3 of section E2 in chapter II are utilized in order to calculate the torque  $M_R$ . It indi-

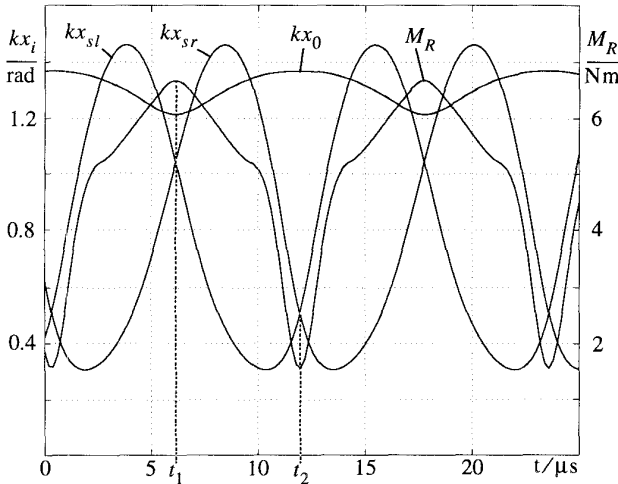


Figure 14: Illustration of the alteration of stick points  $x_{sl}$  and  $x_{sr}$ , half of the contact length  $x_0$  and the drive's torque  $M_R$  for a non ideal traveling wave ( $\varphi_m = -60^\circ, \hat{w}_1 = \hat{w}_2 = 0.8 \mu m$ ).

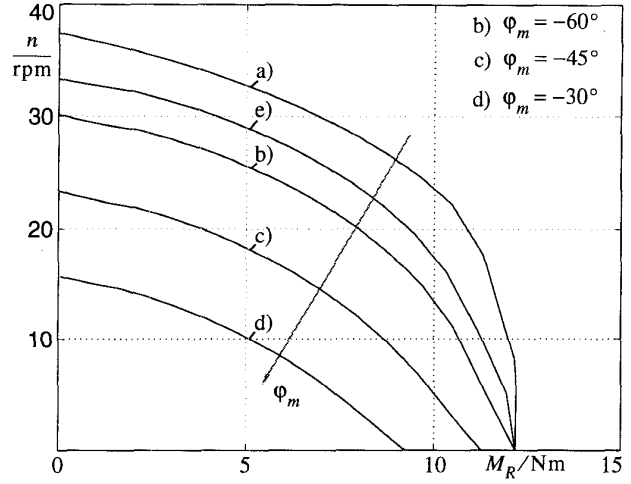


Figure 15: Speed-torque curves for the general case of a non ideal traveling wave: a)  $\varphi_m = -90^\circ$  and  $\hat{w}_1 = \hat{w}_2 = 0.8 \mu m$  (ideal wave)  
b) to d)  $\varphi_m \neq -90^\circ$  and  $\hat{w}_1 = \hat{w}_2 = 0.8 \mu m$   
e)  $\varphi_m = -90^\circ, \hat{w}_1 = 0.96 \mu m$  and  $\hat{w}_2 = 0.64 \mu m$

cates a large torque ripple of about  $5 \text{ Nm}$  (peak to peak) for the simulated non ideal traveling wave and an average value of  $\overline{M_R} = M_L = 5 \text{ Nm}$  at steady state. As remarkable result it is obtained, that the maximum of  $M_R$  occurs together with the minimum of contact zone length  $2x_0$ . This non trivial finding can be explained by the figure of ellipses in Fig. 8 and Fig. 9. According to Fig. 9 a maximum amplitude  $\hat{w}$  is obtained at  $\hat{x} = \lambda/8$  but at the same time  $\hat{v}_h$  becomes minimal. Thus, a wide contact zone  $2x_0$  results at  $t_2$  in Fig. 14 with large braking zones, since  $x_{sl}$  and  $x_{sr}$  are very small. In the opposite case a minimal amplitude  $\hat{w}$  results at  $\hat{x} = -\lambda/8$  in Fig. 9 together with the smallest  $x_0$  in Fig. 14 at  $t_1$ . But in this case  $\hat{v}_h$  is large, so are  $x_{sl}$  and  $x_{sr}$ , resulting in a larger driving zone. In this specific cases  $x_{sl}$  and  $x_{sr}$  are equal, with  $x_c$  identical to zero, characterized by the perpendicular main axis of the ellipses to the surface of the stator, see Fig. 9.

In Fig. 15 speed-torque curves are illustrated for the general case of a non ideal traveling wave. For ideal conditions ( $\hat{w}_1 = \hat{w}_2, \varphi_m = -90^\circ$ ) the highest torque curve results as was expected. With increasing phase deviation from  $\varphi_m = -90^\circ$  as well as for differing amplitudes  $\hat{w}_1 \neq \hat{w}_2$  the speed-torque curve is lowered. The speed-torque curves continues towards the other quadrants and converge to  $M_{R,max} = \pm \mu F_N R_w = \pm 12.18 \text{ Nm}$ . For the reversing mode of the drive the magnitude of the speed-torque curves are identical.

Based on the previous mathematical modeling of the drive a simulative verification of the phenomenons succeeded, which can be observed on the physical drive, operated under non ideal conditions.

#### IV. CONCLUSION

A rotary traveling wave type ultrasonic motor powered by a resonant converter is modeled to optimize the overall drive performance by simulation and to develop suitable control strategies for the drive. After a brief review of modeling rotary, traveling wave type USMs a

two-phase resonant converter, allowing a very flexible control of the drive by which cross couplings and unsymmetries of the motor can be compensated, is modeled taking care of some parasitics of the power electronic circuit. The interaction between the feeding converter and the vibrating system is reflected by an electromechanical two-mode approximation for the piezoceramic and stator based on finite-element methods for the parametrization of the motor. Equipped with recent modeling advances of the nonlinear stator/rotor-contact mechanism an extended contact model is derived for non ideal traveling waves, considering interface forces between stator and rotor. After the integration of the individual modeling aspects into a common signal flow diagram for the total electromechanical system various phenomena observed on physical drives are verified by simulations and explained by graphical means, to ease the insight into the USM's operation principle.

As the total drive scheme is reflected so far by its simulation model, it is projected to verify the results obtained by measurements on a high torque USM under construction in the framework of this project. Recently, first investigations on the dynamic behavior of the ultrasonic drive were started. Then after the development of control schemes the total drive will be optimized based on the simulation model and experiments.

#### ACKNOWLEDGMENT

Thanks to the German Research Council for financing the USM-project, split between the Mechatronics and Robotics Department in cooperations with the Institute for Power Electronics and Electrical Drives (University of Paderborn, Germany).

#### REFERENCES

- [1] T. Sashida, T. Kenjo: An introduction to ultrasonic motors, Clarendon Press - Oxford (1993)
- [2] P. Hagedorn, J. Wallaschek: Travelling wave ultrasonic motors, part I: Working principle and mathematical modelling of the stator. Journal of Sound and Vibration (1992), 155(1), pp. 31-46
- [3] S. Furuya, T. Maruhashi, Y. Izuno and M. Nakaoka: Load-adaptive frequency tracking control implementation of two-phase resonant inverter for ultrasonic motor. IEEE Transactions on Power Electronics, Vol. 7, No. 3, July 1992, pp. 542-550.
- [4] H. Hirata, S. Ueha: Design of a traveling wave type ultrasonic motor, IEEE Transactions on Ultrasonics, Ferroelectrics, and Frequency Control, Vol. 42, No. 2, March 1995, pp. 225-231.
- [5] J. Wallaschek: Piezoelectric ultrasonic motors. Journal of Intelligent Material Systems and Structures, Vol.6, January. 1995, pp. 71-83.
- [6] H. Grotstollen, J. Krome, J. Maas, J. Wallaschek: Systemoptimierung eines geregelten Ultraschall-Wanderwellenantriebes. Zwischenbericht zum DFG-Projekt WA 564/7-1, March 1995.
- [7] A. M. Flynn: Torque production in ultrasonic motors. Private communication, MIT Artificial Intelligence Lab., December 1993.
- [8] X. Cao, J. Wallaschek: Estimation of the tangential stresses in the stator/rotor-contact of travelling wave ultrasonic motors using visco-elastic foundation models, accepted for 2nd Internat. Conf. CONTACT MECHANICS 95, Ferrara, Italy, July 1995
- [9] H. Hirata, S. Ueha: Revolution speed characteristics of an ultrasonic motor estimated from the pressure distribution of the rotor, Proc. 12th Symp. on Ultrasonic Electronics, Tokyo 1991
- [10] N. Hagood, A. Mc Farland: Modeling of piezoelectric rotary ultrasonic motor, IEEE Transactions on Ultrasonics, Ferroelectrics, and Frequency Control, Vol. 42, No. 2, March 1995, pp. 210-224.
- [11] J. Maas, P. Krafka, N. Fröhleke, H. Grotstollen: Prototype drive and modulation concepts for DSP-controlled ultrasonic motors powered by resonant converters, EPE'95, Sevilla, Sept. 1995.
- [12] J. Krome, J. Wallaschek, J. Maas: Models for the electro-mechanical interaction of the stator of a piezoelectric ultrasonic motor and its power supply, contribution on minisymposia „Mathematical modelling of piezoelectric drive systems“, ICAM'95, Hamburg, July 1995.

#### APPENDIX

TABLE I  
Parameters of ultrasonic drive under study

Parameter	Description	Value
$n_T$	Transformation ratio	2
$R'_{inv}$	Resistance of power supply	0.5 $\Omega$
$R'$	Total resistance	4 $\Omega$
$L_s$	Inductance of resonant tank	5.3 mH
$L_m$	Inductance of transformer	9.38 mH
$C_{p1}=C_{p2}$	Capacitances of piezoceramic	3.72 nF
$R_p$	Resistance of piezoceramic	83 k $\Omega$
$\hat{A}_{1,2}$	Elongation factors	$1.75 \cdot 10^{-10}$ m/V
$c_c$	Ceramic stiffness	$2.37 \cdot 10^9$ N/m
$\epsilon_1 = \epsilon_2$	Small symmetry disturbances	2 %
$m$	Model mass of stator and ceramic	0.111 kg
$c_{s1}$	Model stiffness of sine mode	$5.036 \cdot 10^9$ N/m
$c_{s2}$	Model stiffness of cosine mode	$4.99 \cdot 10^9$ N/m
$\Delta c_s$	Unsymmetries in modal stiffnesses	$0.046 \cdot 10^9$ N/m
$d_{s1}$	Equivalent damping of sine mode	477.8 Ns/m
$d_{s2}$	Equivalent damping of cosine mode	476.4 Ns/m
$m_R$	Rotor mass	0.035 kg
$J$	Rotor inertia	$0.1 \cdot 10^{-3}$ kgm <sup>2</sup>
$\lambda$	Wavelength of traveling wave	24.3 mm
$n$	Number of modal diameter	15
$a$	Surface distance	4.5 mm
$c_N$	Equivalent stiffness of contact layer	12000 N/mm <sup>2</sup>
$R_w$	Average radius of contact area	58 mm
$F_N$	Axial force applied to the rotor	700 N
$\mu$	Coulomb's Coefficient of friction	0.3
$M_L$	Torque applied to the rotor	-12 Nm - 12 Nm
$E$	Young's modulus of contact layer	6000 N/mm <sup>2</sup>